

Ducted-Fan Force and Moment Control via Steady and Synthetic Jets

Osgar John Ohanian III^{*}, Etan D. Karni[†],
AVID LLC, Blacksburg, VA, 24060,

W. Kelly Londenberg[‡], Paul A. Gelhausen[§]
AVID LLC, Yorktown, VA, 23692

ajohand

Daniel J. Inman^{**}

Virginia Polytechnic Institute and State University, Blacksburg, VA, 24060

The authors have explored novel applications of synthetic jet actuators for leading and trailing edge flow control on ducted fan vehicles. The synthetic jets on the duct are actuated asymmetrically around the circumference to produce control forces and moments. These forces and moments could be utilized as flight control effectors for combating wind gusts or reducing control surface allocation required for trimmed flight. Synthetic jet component design, vehicle integration, CFD modeling, and wind tunnel experimental results are presented with a comparison to steady blowing. The flow control concepts demonstrated production of aerodynamic forces and moments on a ducted fan, although some cases required high flow rate steady blowing to create significant responses. Attaining high blowing momentum coefficients from synthetic jets is challenging since the time-averaged velocity is only a function of the outstroke: from bench test experiments it was seen that the time-averaged velocity was roughly one fourth of the peak velocity observed during the outstroke. The synthetic jets operated at lower blowing momentum coefficients than the steady jets tested, and in general the ducted fan application required more flow control authority than the synthetic jets could impart. However, synthetic jets were able to produce leading edge separation comparable to that obtained from steady jets with much higher blowing coefficients.

Nomenclature

A_{duct}	=	Duct planform area, $D \cdot c$
A_{disc}	=	Fan disc area, $\pi \frac{D^2}{4}$
a_j	=	Jet orifice area
C_m	=	Pitching moment coefficient, based on fan speed, $\frac{M_y}{\rho N^2 D^5}$
C_X	=	X Force coefficient, based on fan speed, $\frac{F_x}{\rho N^2 D^4}$
C_Z	=	Z Force coefficient, based on fan speed, $\frac{F_z}{\rho N^2 D^4}$

^{*} Aircraft Design Engineer, AVID LLC, Blacksburg, VA / Ph.D. Student, Mechanical Engineering, Virginia Tech, Blacksburg, VA, AIAA Member.

[†] Aircraft Design Engineer, AVID LLC, Blacksburg, VA, AIAA Member.

[‡] Senior Aircraft Design Analyst, AVID LLC, Yorktown, VA, Senior AIAA Member.

[§] CTO, AVID LLC, Yorktown, VA, AIAA Senior Member.

^{**} George R. Goodson Professor, Mechanical Engineering, Virginia Tech, Blacksburg, VA, AIAA Fellow.

ΔC_m	= Incremental Pitching moment coefficient due to jet actuation
ΔC_X	= Incremental X Force coefficient due to jet actuation
ΔC_Z	= Incremental Z Force coefficient due to jet actuation
c_μ	= Jet momentum coefficient, $\frac{\dot{m}_j U_j}{q_{duct} A_{duct}}$ for steady jets, $\frac{n \bar{I}_j}{q_{duct} A_{duct}}$ for synthetic jets
c	= Duct chord
c_s	= Speed of sound
D	= Duct inside diameter (fan diameter)
D_j	= Jet cavity diameter
F_X	= Force in body-fixed X direction
F_Z	= Force in body-fixed Z direction
f	= Synthetic jet drive frequency
f_H	= Helmholtz frequency
H_j	= Jet cavity depth
h_j	= Jet orifice depth
\bar{I}_j	= Time averaged momentum during outstroke, $\frac{1}{\tau} \rho l_j w_j \int_0^\tau u_j^2(t) dt$
L_0	= Jet slug length, $U_0 T$
L	= Non-dimensional jet slug length, L_0/w
l_j	= Jet orifice slot length
M_Y	= Pitching moment about body-fixed y-axis
\dot{m}_j	= Steady jet mass flow rate
n	= Number of jet slots
N	= Rotational speed of fan in revolutions per second
q_∞	= Free-stream dynamic pressure
q_{duct}	= Dynamic pressure inside duct due to induced velocity
Re_{U_0}	= Synthetic jet Reynolds number, $\frac{U_0 w_j}{\nu}$
T	= Thrust
T_{jet}	= Period of jet cycle
u_j	= Centerline jet velocity
U_{Peak}	= Phase averaged peak centerline jet velocity
U_0	= Time averaged jet velocity over cycle, $\frac{1}{T} \int_0^{T/2} u_j(t) dt$
U_j	= Spatially averaged steady jet velocity
V_∞	= Free-stream velocity
$V_{induced}$	= Velocity induced by fan
V_R	= Velocity ratio, U_0/V_∞
w_j	= Jet orifice slot width
α	= Angle of Attack
ρ	= Air density
τ	= Jet out-stroke time, $T/2$
ν	= Kinematic viscosity

I. Introduction

SYNTHETIC Jet Actuators (SJA) have generated considerable research interest due to their potential use in applications where steady blowing flow control is not feasible [1]. One such application is active flow control in unmanned air vehicles (UAVs). Depending on the scale of such aircraft, there may not be available volume or weight/power budget to implement a traditional flow control scheme. The advent of “zero net mass flux” actuators (another name for SJAs) has theoretically eliminated this hurdle; however, many technical issues must be overcome to successfully implement a system that can meet the performance requirements as well as weight, size, and power constraints of a UAV. This paper explores the use of steady and synthetic jets on a ducted fan vehicle to create forces and moments for flight control. The sections cover the synthetic jet component design, vehicle integration, CFD modeling, and experimental results from wind tunnel and static tests, with a comparison to steady blowing.

A. Ducted Fan Background

A ducted fan produces more thrust than a fan (propeller) of the same diameter in isolation [2]. This is due to the thrust/lift produced by the duct lip. In general, the pressures on the duct surface created by the flow induced by the fan are a large contribution to the overall forces and moments on the ducted fan unit. In particular, the high-speed flow into the duct induced by the fan causes a low-pressure region on lip. This phenomenon results in a net force in the thrust direction during hover and can produce lift and pitching moment in forward flight [3]. Under certain conditions the flow over the duct lip can separate, affecting the thrust, lift, and pitching moment. It is a complex problem that depends on lip geometry, angle of attack, free stream velocity, and fan rpm [4],[5]. In general, ducted fans experience large nose-up pitching moments during transition from hover to cruise (low speed and high angle of attack), and the objective of the concepts investigated is to reduce the pitching moment of the vehicle under these conditions in a controlled manner. This reduction in pitching moment would allow for lower control surface allocation during transition to forward flight and would improve wind gust rejection performance.

B. Flow Control Concepts

If the flow over the duct surface can be controlled—i.e. flow turned, accelerated, separation eliminated or produced on demand—then a ducted-fan vehicle could be optimized for combating gusting winds. Asymmetric lift from one side of the duct having attached flow while the opposite side is separated could be used as a control moment or to alleviate undesirable moments due to wind gusts. On the other hand, achieving attached flow on the entire duct during a typical stall condition could enhance vehicle performance and efficiency. The concepts investigated herein use separation on the leading edge to affect thrust and pitching moment, and a Coanda surface at the trailing edge to create normal force and reduce pitching moment. In the first concept, applying the jet flow against the natural flow over the duct lip, the jets cause the flow to separate; when the jets are turned off, the flow naturally reattaches. This concept is shown in Figure 1. This separation can decrease the pitching moment experienced during wind gusts and could reduce the amount of flight control actuator usage to maintain stable flight.

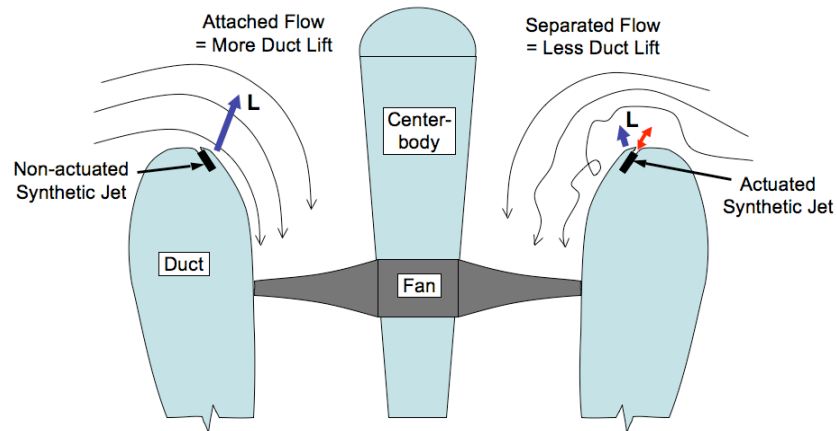


Figure 1: Duct Lip Synthetic Jet Flow Control

In the second concept, the duct trailing edge is replaced by a Coanda surface geometry with a bluff step. When the synthetic jet emanating from the step is turned on it causes the flow to stay attached to the Coanda surface, thereby causing the primary flow out of the duct to turn. This results in a normal force opposite to the turned flow and a corresponding moment about the vehicle CG. When the jet is turned off the flow separates off the bluff corner and the flow proceeds straight out of the duct. This concept is shown in Figure 2.

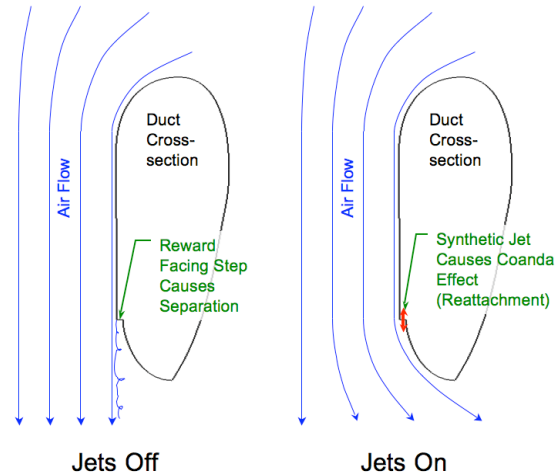


Figure 2: Duct Trailing Edge Synthetic Jet Flow Control

A novel use of these two flow control concepts is to apply the control asymmetrically to the duct in order to produce an imbalance in forces, thus resulting in a moment. The net force and moment caused by the asymmetric flow control could be used to control or augment the motion of a ducted fan vehicle. The target condition for affecting pitching moment is trimmed horizontal flight at 35 ft/s free-stream velocity with -20° angle of attack (tilt into the wind).

Steady blowing has been investigated for ducted fan control forces and moments in hover [6] and to enhance shrouded propeller static thrust [7],[8]. This present effort investigates the effects of synthetic and steady jets for hover as well as forward flight conditions over a large range of angles of attack. Other researchers have investigated synthetic jets on the stator blades of a ducted-fan to control vehicle rotation about the propeller axis [9], but controlling the flow over the duct surface here presents a larger opportunity for affecting the overall vehicle aerodynamics. Comparisons between steady and unsteady (synthetic) jets in isolation have been documented [10], but it is the intent of this paper to compare steady and unsteady blowing in a specify application of flow control.

II. Synthetic Jet Component Design

A component development effort was undertaken to design and bench test synthetic jet actuators based on flight-size piezoelectric elements (27mm APC FT-27T-3.9A1) to identify anticipated jet velocities for vehicle wind tunnel testing. The element selected is mass-produced for use as a piezoelectric buzzer and consequently is relatively inexpensive (roughly \$1 each). This element has been used by other researchers to produce a jet velocity of 420 ft/sec for a 0.05" circular orifice in a normal orientation configuration (jet perpendicular to diaphragm) [11]. One of the objectives of this test was to quantify the expected jet velocities for a laterally oriented (jet parallel to diaphragm) rectangular slot with orifice area more than ten times greater. A long slot orifice is more applicable to the tangential flow control concepts investigated for the ducted fan application. The bench test setup is shown in Figure 3, with a schematic of the cavity layout with the slot length dimension going into the page.

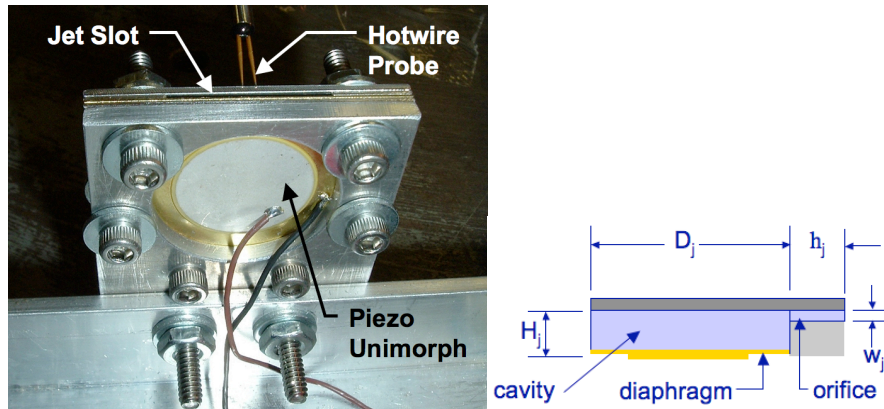


Figure 3: (left) Close-up of Experimental Setup for Synthetic Jet Testing, (right) Schematic of Lateral Jet Cavity Layout

The input voltage limits used for the piezoelectric diaphragm are ± 150 V. Jet velocities were measured with a Dantec 55M01 anemometer with TSI hotwire probe 1210-T1.5. Hotwire anemometers can measure velocities at frequencies up to 50 kHz, and is therefore a favored instrument for measuring SJA flows. The anemometer was calibrated over the range of expected jet velocities (0 to 300 ft/sec), and a fourth order polynomial was used to translate output voltage to air velocity. The hotwire probe (approximately 0.08" long filament, microns in diameter) was positioned at the center of the slot orifice width and length, one slot width away in the axial direction. Other researchers have recognized this practice as a sufficient method to characterize and compare SJA performance [11]. A dSPACE™ data acquisition system with SIMULINK™ integration was used to run the experiments, automate tests, and collect data. A Trek 50/750 power supply/amplifier was used to generate the high voltages (± 150 V) necessary for the piezoelectric elements, but was limited in current to 50 mA. Figure 4 shows the overall setup.

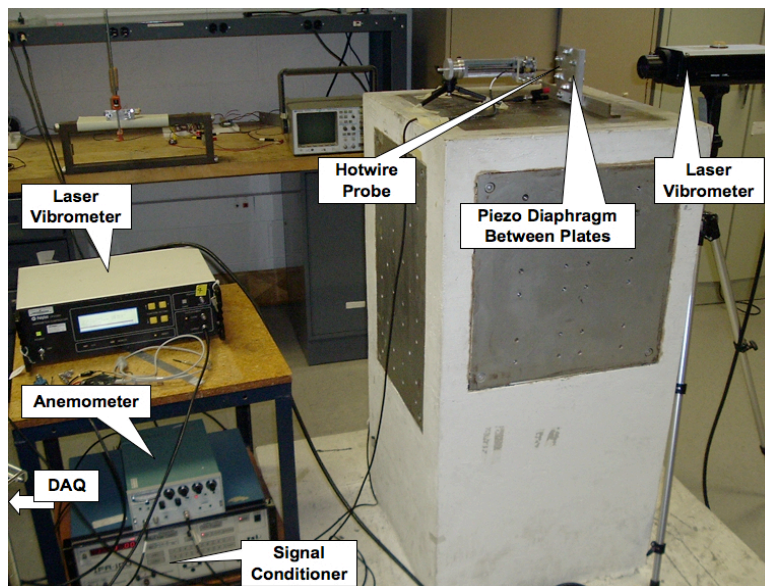


Figure 4: Synthetic Jet Bench Test Experimental Setup

C. Experimental Results

Synthetic jet output is very dependent on actuation frequency. Two main frequencies dominate their behavior: the Helmholtz frequency of the cavity, and the damped natural frequency of the mechanical diaphragm. At the Helmholtz frequency and above, the air in the cavity exhibits compressibility [12]. The relative order of the natural frequency of the diaphragm being above or below this frequency dictates what kind of behavior is exhibited. The general finding of this research and other researchers is that the natural frequency of the mechanical diaphragm

element is more influential than the Helmholtz frequency in producing the highest jet velocities [11]. Further benefit to jet output can be attained by designing the cavity and diaphragm to align the mechanical natural frequency and Helmholtz resonance frequency [12]. This was not practical for the implementation needed for this flow control application, given the space constraints and chosen diaphragm element. In all of the cases tested the damped natural frequency of the diaphragm was below the Helmholtz frequency of the cavity, and produced significantly higher jet output than driving at the Helmholtz frequency. A summary of the cases tested is shown in Table 1, with the corresponding Helmholtz frequency for the specified geometry. The Helmholtz frequency is defined by Eq. (1). In all cases the diameter of the cavity, D_j , was constant.

Table 1. Summary of Test Case Parameters

Orifice Type	D_j (in)	H_j (in)	Volume (in ³)	l_j (in)	w_j (in)	h_j (in)	Helmholtz Freq (Hz)
0.03" x 0.8" Slot	1	0.05	0.039	0.8	0.03	0.1	5269
0.03" x 0.8" Slot	1	0.06	0.047	0.8	0.03	0.1	4810
0.03" x 0.8" Slot	1	0.07	0.055	0.8	0.03	0.1	4453
0.03" x 0.8" Slot	1	0.08	0.063	0.8	0.03	0.1	4166
0.02" x 0.8" Slot	1	0.06	0.047	0.8	0.02	0.1	3927
0.04" x 0.8" Slot	1	0.06	0.047	0.8	0.04	0.1	5554

$$f_H = \frac{c_s}{2\pi} \sqrt{\frac{a_j}{h_j V_{cavity}}} \quad (1)$$

After using a sweep of driving frequency to identify the range of the diaphragm damped natural frequency (via a ‘chirp’ signal), a detailed investigation near the frequency of interest was performed for each configuration. Automated test sweeps were utilized to collect jet velocity data for a range of frequency, voltage, and driving waveform. This procedure was applied to different configurations of jet geometry including cavity depth and orifice width. Figure 5 shows the results of this process for several cavity depths with constant orifice geometry: a 0.030" x 0.8" rectangular slot.

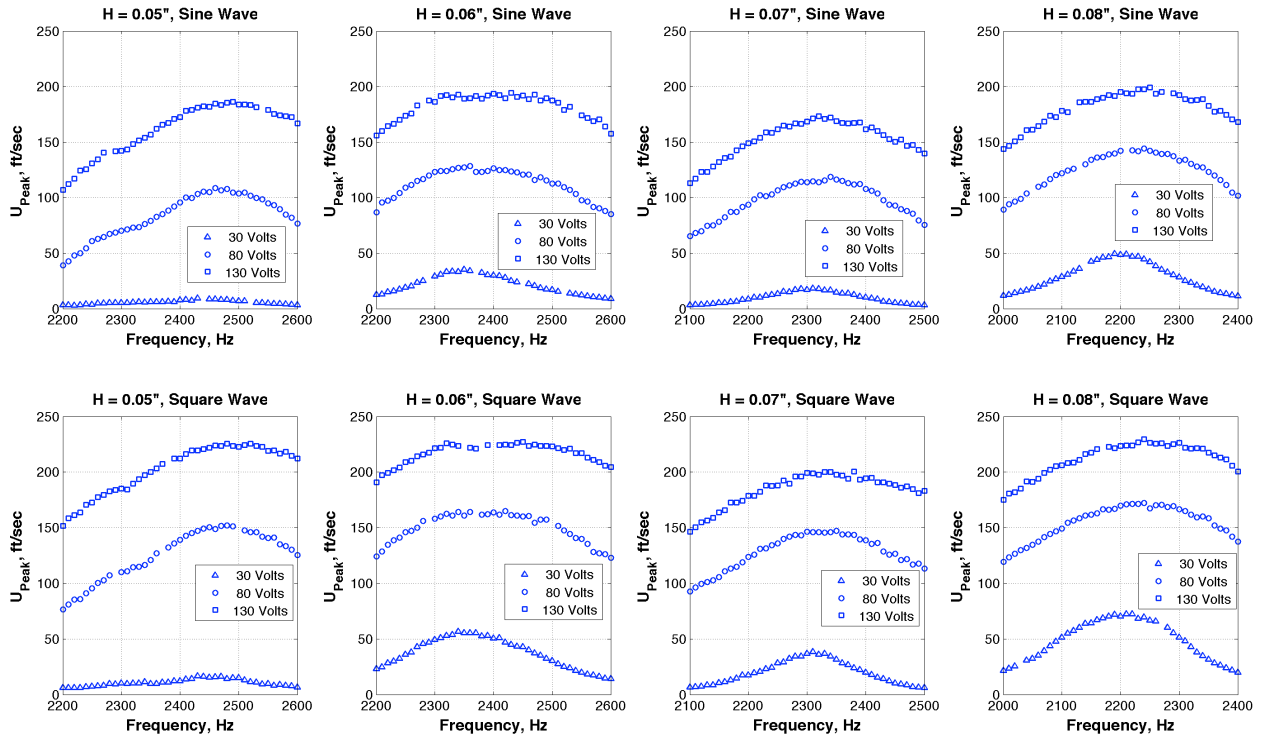


Figure 5: Frequency, Voltage, and Waveform Sweep for Various Cavity Depths for Fixed Slot Width of 0.03"

These results show that there is only a slight sensitivity in peak jet velocity due to cavity depth. One noticeable difference due to cavity depth is the frequency at which the peak velocity occurs. This frequency is essentially the damped natural frequency of the piezoelectric diaphragm. As the cavity depth and volume increase, the damped natural frequency decreases. This implies greater damping or losses for larger cavities, and may imply that shallower cavities are superior. From a space and packaging standpoint, this is a positive finding. The peak jet velocity observed from this data is 225 ft/sec for a 130V amplitude square wave input at 2400 Hz for a cavity depth of 0.06".

The effect of orifice slot width was explored while using a constant cavity depth of 0.06". The general trend is that the widest slot produced the lowest peak velocities. To take a closer look at this trend, only the highest voltage square wave results are superimposed for comparison in Figure 6.

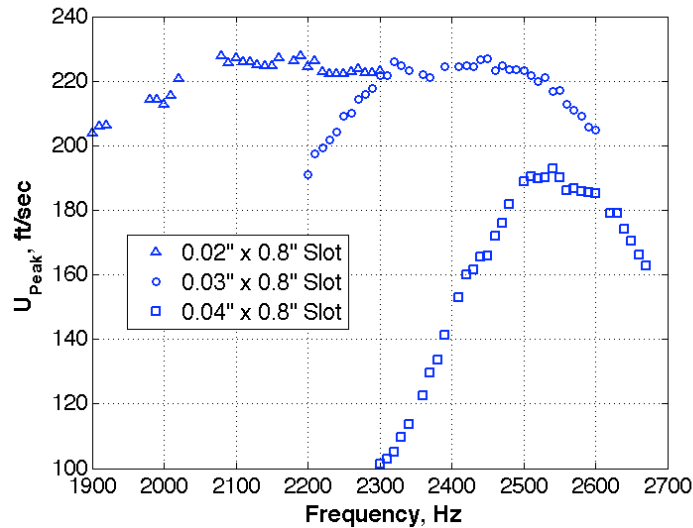


Figure 6: Effect of Orifice Width on Peak Jet Velocity Characteristics

The widest slot tested, 0.040", showed the lowest peak velocity. This makes sense conceptually: for a given volume displacement or mass flow, the velocity is inversely proportional to exit area. If this trend applied indefinitely, the smallest area slot (0.020") would show significant increases over the 0.030" slot, but this is not observed. The 0.020" and 0.030" slots produce nearly the same peak velocities, although at different frequencies. This is attributed to losses building up as the orifice width decreases, and is supported by the decrease in damped natural frequency. This implies that there is an optimal jet width for any synthetic jet design that balances orifice losses with orifice area. If the slot width decreased to values smaller than 0.020" it is anticipated that the overall jet velocity would decrease due to losses. For this setup the optimum width was ascertained to be in the realm of 0.020" to 0.030". For wind tunnel vehicle testing, the 0.030" width slot was selected for two reasons: first, it is easier to fabricate within tolerances; and second, since it attains roughly the same velocity with a larger area it will impart more momentum to the flow.

The difference in jet performance based on driving voltage waveform can be observed in Figure 7. The results show that a square wave driving function produce roughly a 20% increase in peak jet velocity over a sinusoidal input.

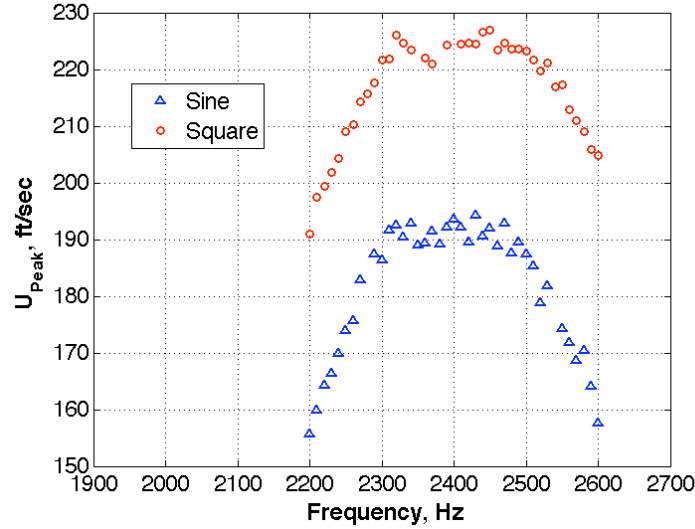


Figure 7: Effect of Driving Waveform on Peak Jet Velocity

It should be noted that the square wave was the input to the high voltage amplifier, and that only after further investigation measuring the voltage and current entering the piezoelectric diaphragm was it found that the output of the amplifier (which was current limited) was more sinusoidal in form. The square wave input merely increased the current amplitude. Driving a capacitive piezoelectric diaphragm with a near square wave input would result in very large currents, especially while driving it at its natural frequency. Square wave inputs are more wearing on the diaphragm and also tend to excite higher frequency harmonics that are not beneficial. The first bending mode of the diaphragm produces the most jet output, due to that mode creating the largest volume displacement. Therefore, sinusoidal waveforms that maximize voltage and current amplitude within the constraints of the drive electronics and durability of the piezoelectric element will result in the highest sustainable jet outputs.

An example of the centerline jet velocity, input voltage, and input current to the synthetic jet is shown in Figure 8 for a sinusoidal input of 2300 Hz.

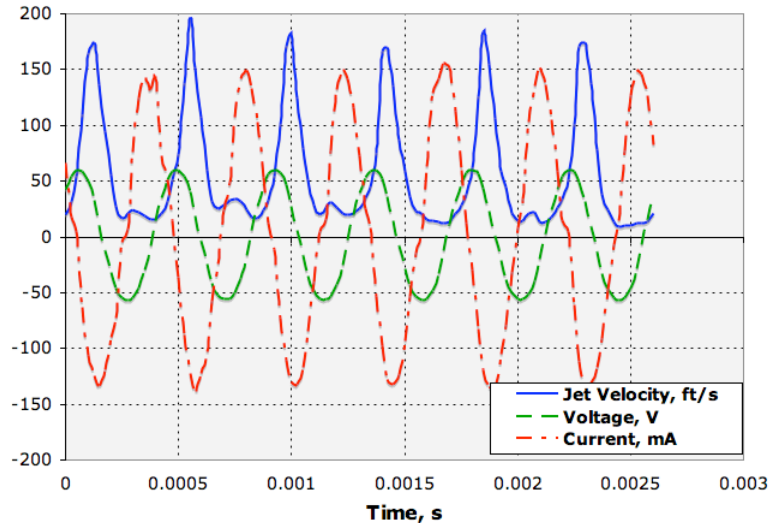


Figure 8: Jet Velocity, Input Voltage, and Input Current Signals for 2300 Hz Sinusoid Drive Waveform

The parameters for this dataset are representative of those used in the vehicle wind tunnel tests. The peak jet velocities observed are in the vicinity of 200 ft/s. Integrating the centerline velocity over the outstroke according to Equation (2) from Holman et. al. [13] results in a time averaged velocity, U_0 , of 49.8 ft/s and stroke length, L_0 , of 0.26". The dimensionless stroke length L_0/w_j for this case is 8.7. Note that the time-averaged velocity, which is used

in flow control application calculations, is roughly one fourth of the peak jet velocity. This makes it difficult to attain high blowing momentum coefficients, as will be seen later.

$$U_0 = fL_0 = f \int_0^{T/2} u_j(t) dt \quad (2)$$

Using this velocity and adapting the Reynolds number equation from [13] to employ slot width instead of diameter, as seen in Equation (3), results in a value of 818.

$$\text{Re}_{U_0} = \frac{U_0 w_j}{\nu} \quad (3)$$

The inverse of the Strouhal number (a function of Reynolds and Stokes numbers) adapted from [13] to use jet width and Re_{U_0} is depicted in Equation (4). A value of 2.75 was attained for the data presented and is representative of the jet performance as installed in the vehicle model. This value is well above the jet formation criterion of 0.16 as predicted by [13].

$$\frac{1}{Sr} = \frac{(L_0/w_j)}{\pi} = \frac{2U_0}{\omega w_j} = \frac{(2U_0 w_j/\nu)}{(\omega w_j^2/\nu)} = \frac{2\text{Re}_{U_0}}{S^2} \quad (4)$$

D. Synthetic Jet Component Design Summary

Peak jet velocities of 200 to 225 ft/sec were attained with slot and cavity geometry and orientation similar to the anticipated application. A slot width of 0.030" was chosen for going forward into wind tunnel model design and testing. Also, it was found that shallower cavity depths were desirable from a jet performance standpoint, but this fact also aids in packaging such actuators in a vehicle with limited volume for components.

III. Synthetic Jet Actuator Vehicle Integration

One of the challenges in developing the wind tunnel vehicle model was the integration of the piezoelectric diaphragm elements. Three main criteria drove the design of the wind tunnel model SJA installation. These were:

1. Minimize lateral spacing between SJA, to more closely approximate a uniform jet along the entire circumference of the duct.
2. Provide consistent clamping loads for each SJA, to improve boundary condition uniformity.
3. Securely but non-permanently install the piezoelectric diaphragms in the model. This is necessary to minimize downtime from any failures encountered during the wind tunnel test.

The final concept selected was the axial screw clamp, shown below in Figure 9 and Figure 11. While it requires slightly more parts than other options, it allows for simple replacement of elements, has excellent adjustability, and yields minimum lateral spacing between SJA thereby increasing the coverage of the duct circumference. For a flight implementation, the piezoelectric elements would be directly bonded into the cavity to minimize volume and weight.

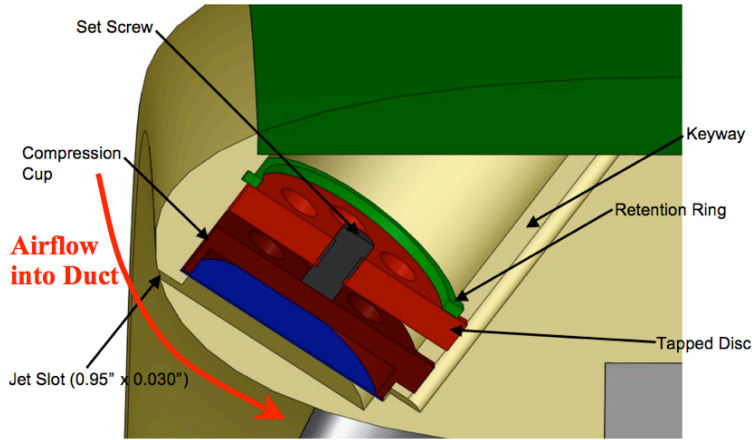


Figure 9: Piezoelectric Diaphragm Mounting for Leading Edge Blowing Configuration

Figure 9 shows how the jet and cavity are oriented in the duct lip, with the outside of the duct towards the top of the figure. The flow would proceed into the duct, and the jet orifice is oriented to oppose this flow at roughly 45° . The internal parts of the wind tunnel model that housed the piezoelectric diaphragms were machined aluminum, with bored holes to hold the elements. A compression cup presses down on the edge of the piezoelectric diaphragm to apply a uniform clamping load. A tapped disc with setscrew is then inserted, with a retention ring finally snapping into place to support the tapped disc. The setscrew is advanced to push on the compression cup and apply the necessary clamp load uniformly to the diaphragm edge. The added benefit of this approach was that a single input (screw torque) was used to tune the boundary condition for the piezoelectric elements. The coverage of the duct lip attained for the leading edge blowing is 75%, as can be seen in Figure 10.

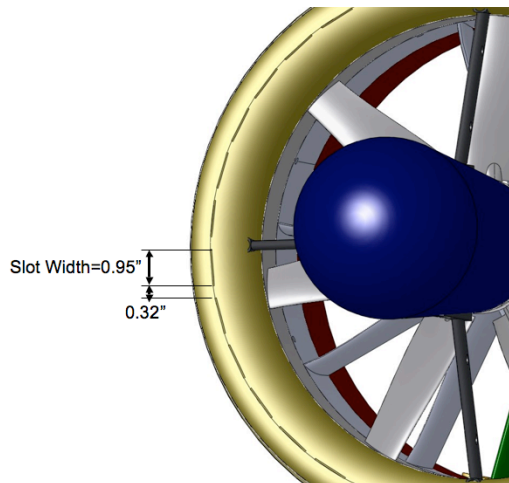


Figure 10: Leading Edge Jet Coverage

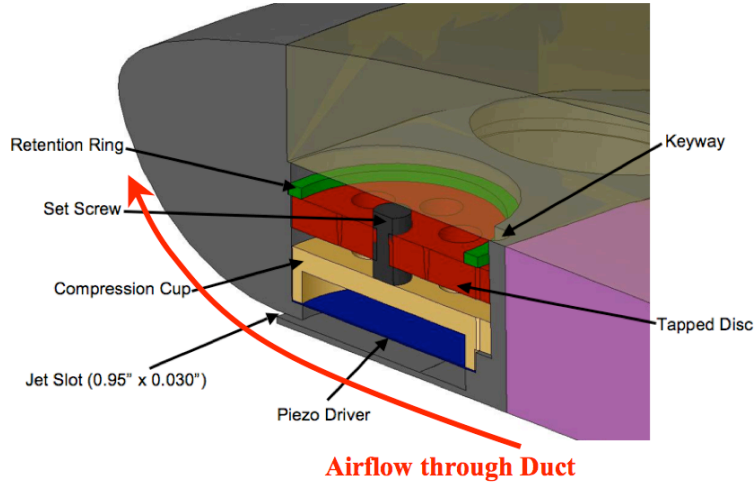


Figure 11: Piezoelectric Diaphragm Mounting for Trailing Edge Blowing Configuration

The trailing edge geometry aligns the jet orifice tangential to the Coanda surface to blow in the same direction as the flow through the duct. To minimize the travel from the cavity to the orifice opening the jet cavity is positioned parallel to the duct inside wall (towards the bottom of the figure). The internal features to hold the piezoelectric elements are identical to the leading edge geometry. The jet coverage attained on the Coanda surface is 85% as seen in Figure 12.

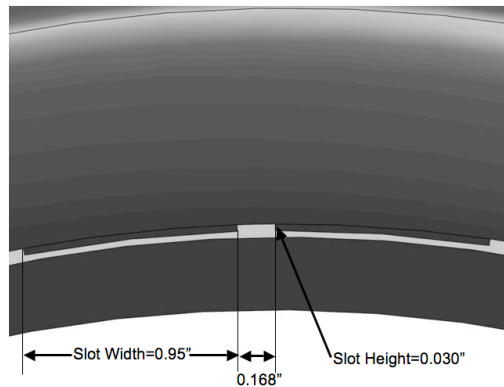


Figure 12: Trailing Edge Coanda Surface Jet Coverage

IV. CFD Modeling of Steady and Unsteady Flow Control on Ducted Fan

A. CFD Solver and Method

Once the synthetic jet actuator design was integrated into the vehicle geometry, 3D time-accurate (unsteady) computational fluid dynamics (CFD) was used to assess the predicted performance and improve the integrated design before fabricating the model geometry. The effect of steady and synthetic jet blowing on the ducted fan configuration was analyzed using the NASA Langley FUN3D Reynolds-averaged Navier-Stokes, unstructured mesh method [14]. Incompressible solutions were obtained for the ducted fan configuration at 15-knots and 14.33° tilt from vertical (-14.33° angle of attack). In each of the CFD solutions, the fan was simulated as an actuator disk, using the rotor method integrated with the FUN3D solver [15]. Using blade geometry and airfoil aerodynamics, this actuator disk method iterates the swirl and pressure increase due to the fan with the computed inflow, resulting in a good simulation of first order fan effects. Steady and unsteady blowing conditions were applied as velocity boundary condition at the orifice. A detailed accounting of the CFD studies would be appropriate for a separate paper, but a summary of the findings and examples of the analysis will be included here.

B. Leading Edge Blowing Analysis

For these studies, the blowing boundary condition was applied at the exit face of the slot, Figure 13. This reduced order modeling allowed for solution convergence, and three blowing velocities were analyzed: 50-ft/sec, 100-ft/sec, and 200-ft/sec. Comparing the 100-ft/sec and 200-ft/sec blowing with the no blowing case, Figure 13, shows that leading-edge blowing is separating the flow over the lip as intended. When the blowing is not present, the flow proceeds into the duct smoothly as desired. As blowing velocity is increased, the core of the separated region is lifted farther off the surface. Also, as blowing velocity is increased, the effect on the vehicle pitching moment is increased. The 50-ft/sec blowing velocity reduced the no blowing configuration pitching moment by more than a third, 100-ft/sec blowing reducing it by half, and 200-ft/sec blowing reducing the no-blowing pitching moment by two-thirds. An interesting observation is that the difference in pitching moment between full (360 deg) circumferential blowing and windward blowing (front 180 deg of duct circumference) was minimal, implying that the majority of the effect on the flow is occurring at the windward lip. Blowing over the leeward half alone produced little effect.

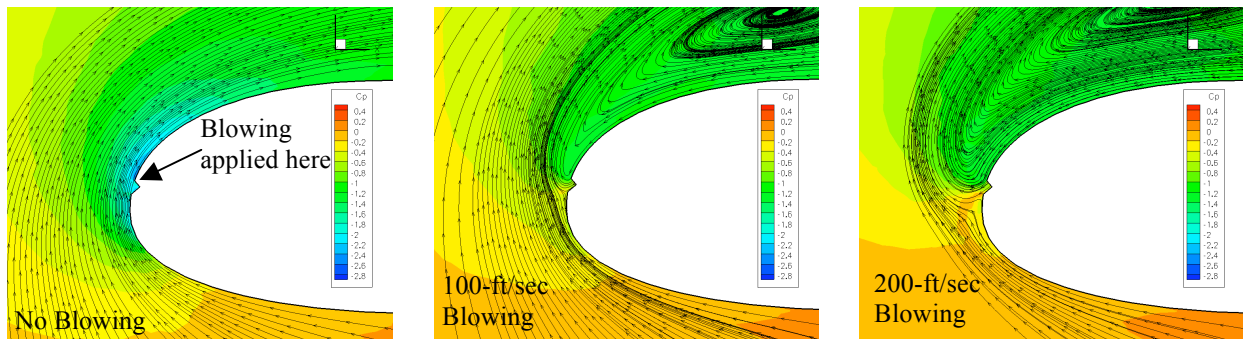


Figure 13: The a5b45 leading-edge blowing geometry results in separated flow over the lip

C. Coanda Trailing Edge Surface Analysis

A trailing edge geometry was developed for a 0.03” slot width and Coanda surface, Figure 14. In initial steady-state analyses, the jet velocity was imposed at the slot exit plane, i.e., the internal slot geometry was not modeled. In these cases, the internal orifice geometry was modeled with the sinusoidal velocity boundary condition applied at the beginning of the orifice neck. Steady blowing over the windward trailing edge at 200 ft/sec resulted in a normal force and decreased the pitching moment. Although the expansion of the streamtube resulted in an expected loss of thrust, power required by the fan also decreased.

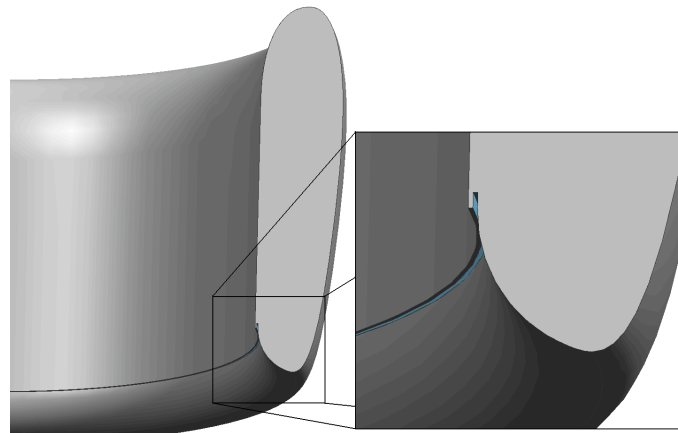


Figure 14: Coanda Trailing Edge Geometry with 0.03” Jet Width and Coanda Surface

Jet velocity was modeled as a time varying sinusoidal function. The 2400-Hz, ± 200 -ft/sec normal sinusoidal velocity boundary condition (values taken from bench test performance) was modeled over 100 computational time steps. It was also determined that little difference in pitching moment was obtained between blowing over half of the trailing-edge circumference and a quarter of the trailing-edge circumference, centered about the windward edge.

Due to the obvious fabrication benefits of instrumenting only a quarter of the duct trailing edge versus half of the circumference, many of the analyses have been conducted for the quarter blowing geometry.

Initial unsteady results exhibited a region of significant flow separation on the Coanda surface. In these analyses, the slot geometry was modeled with an edge normal to the flow inside the duct. The thin wall between the jet throat and the duct flow had square corners. It was determined that the sharp corner was making it difficult to attain attachment on the Coanda surface, so the thin wall geometry was modified to round the corner closest to the duct flow. Analysis of the modified geometry shows the flow remaining attached along more of the Coanda surface curvature, Figure 15.

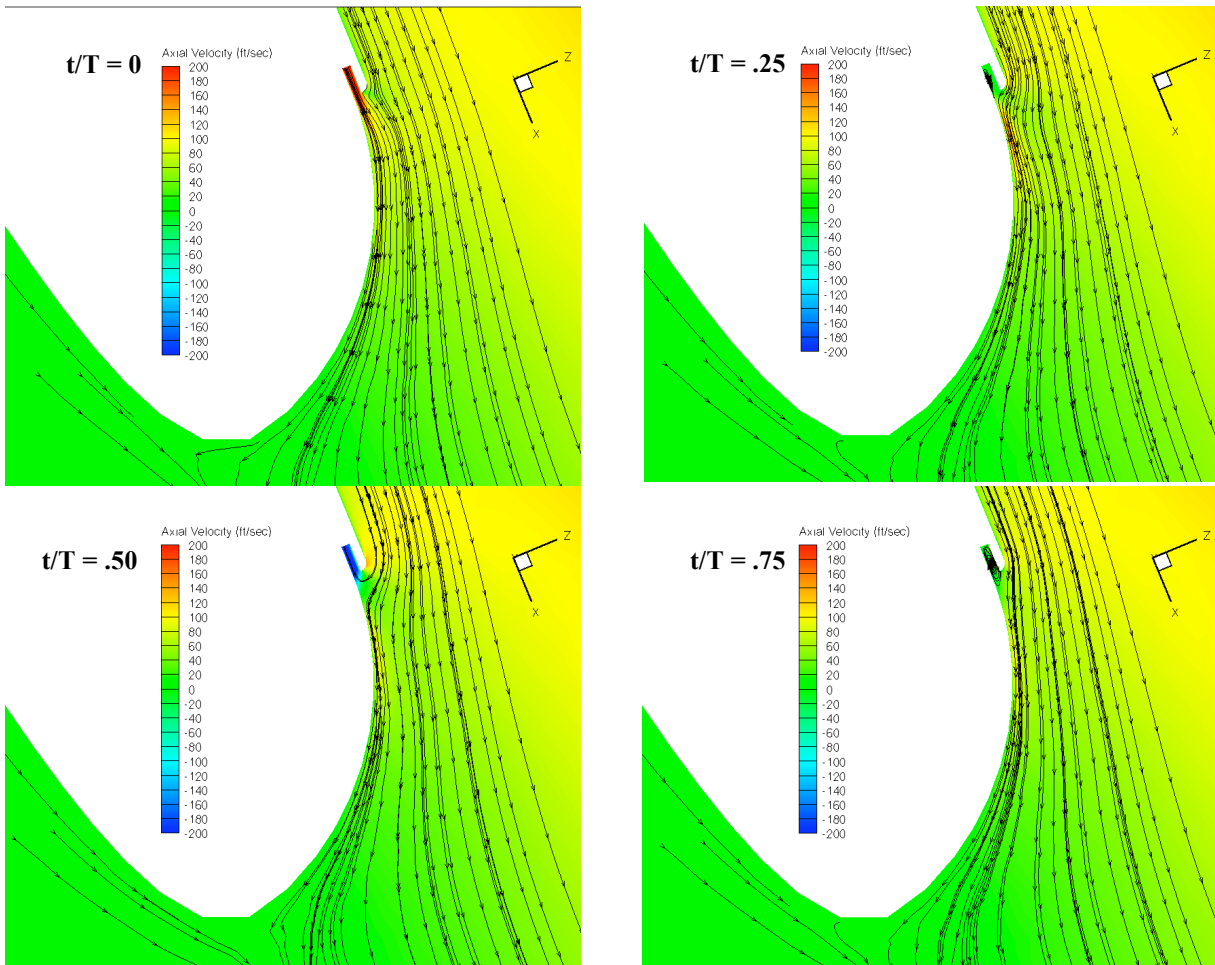


Figure 15: Unsteady CFD Solution for Synthetic Jet Trailing Edge Coanda Flow Control

The red color in the jet orifice corresponds to the outstroke of the synthetic jet ($t/T = 0$) and the blue denotes the in-stroke or suction phase of the synthetic jet ($t/T = 50$). The slug of flow that is pushed out during one cycle of the synthetic jet can be observed in subsequent frames (the warm colors moving down the Coanda surface), and is still observable at $t/T = 75$ close to the time of the next outstroke. With flow remaining attached to the Coanda surface, the streamtube is expanded and turned, with a corresponding normal force and reduction in pitching moment. The rounded corner design was chosen for the wind tunnel experiments. The CFD analysis was helpful in refining the flow control geometry as preparation for wind tunnel experiments.

V. Experimental Setup and Procedure

Static (hover) tests were performed in a high bay area and wind tunnel tests were performed in the Virginia Tech 6ft x 6ft Stability Wind Tunnel. The vehicle model was fabricated from machined aluminum and nylon as well as rapid prototyped resin parts. The model was supported by a 6-component force and moment balance in a side mount

orientation to align the most sensitive channel of the balance with the vehicle's pitching moment axis (y-axis). Pitch sweeps were executed by rotating the wind tunnel turntable on which the balance is mounted, with the direction of flight in the positive x-direction (when angle of attack is zero). An illustration of the balance and vehicle are shown in Figure 16 along with the coordinate system used for collecting data. The data presented herein is transformed to move the moment reference center to the center of the duct lip as a simple datum for the vehicle design. Figure 17 illustrates this coordinate system along with the angle of attack convention (similar to a helicopter). In this coordinate system the vehicle thrust results in a negative F_z force, a traditional normal force corresponds to a negative F_x force, and a nose-up moment is a positive M_y moment.

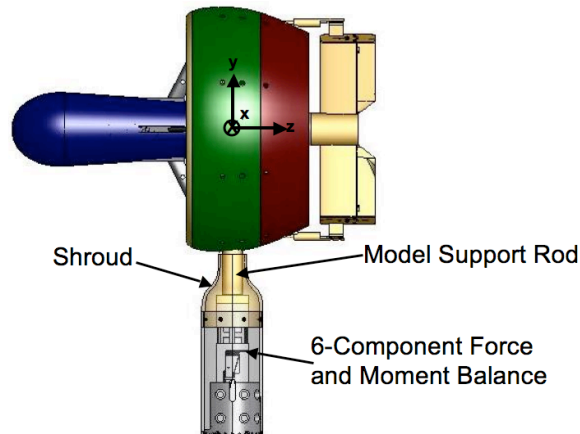


Figure 16: Balance Mounting of Wind Tunnel Model

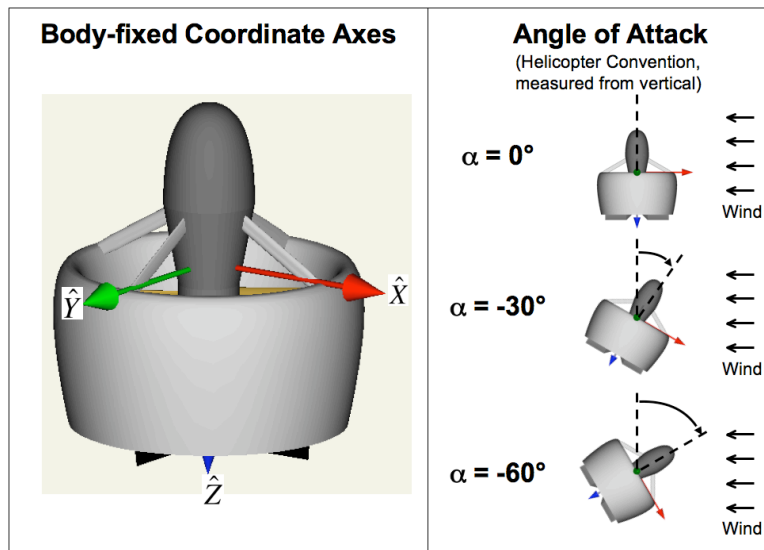


Figure 17: Body-Fixed Coordinate System and Angle of Attack Convention

Multiple configurations of the vehicle model were used to explore the effects of the synthetic jets as well as steady blowing using a compressed air supply. Synthetic jet velocities in the vehicle slots were measured statically with the hotwire anemometry as described in a previous section. The trailing edge peak velocities were comparable to bench test results (~200 ft/s), but leading edge peak velocities were roughly 60% of the bench test values. This was attributed to the orifice depth being longer (due to manufacturing constraints) and the increased losses resulted in a lower jet output and damped natural frequency. The optimum drive frequency for trailing edge actuation was 2300 Hz and for leading edge actuation was 1900 Hz. Steady blowing velocities were set using a mass flow meter. Steady blowing velocities included 164 ft/s, 311 ft/s, and 509 ft/s. The leading edge blowing and trailing edge blowing configurations used to quantify the effectiveness of the synthetic jet actuators are shown in Figure 18. Only eight of the slots were employed in tests, accounting for one quarter of the duct circumference.

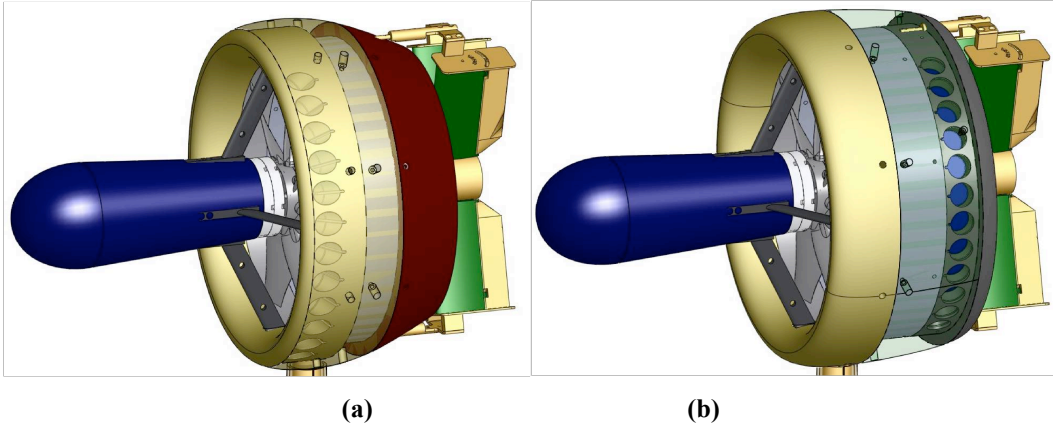


Figure 18: (a) Leading Edge Blowing, (b) Trailing Edge Coanda Blowing

The model was constructed in a modular fashion such that various control surfaces, duct lips and trailing edges could be tested using the same apparatus. The model was installed in the Virginia Tech Stability Wind Tunnel, and is pictured below in Figure 19. The balance and stand rotate on a turntable, so the vehicle is mounted on its side to be able to evaluate a pitch sweep via turntable rotation.



Figure 19: Vehicle Model Installed in Virginia Tech 6 ft x 6 ft Wind Tunnel

Figure 20 shows the Coanda trailing edge component installed in the vehicle, with a close-up view of the curved 0.030" slot geometry. The leading edge and trailing edge flow control components were both machined from aluminum, and EDM (electrical discharge machining) was employed to obtain precise slot geometry. Finally the components were anodized to electrically isolate the piezoelectric components from the rest of the model.



Figure 20: Coanda Trailing Edge Flow Control, with Close-up of Slot Geometry

Figure 21 shows the leading edge flow control duct lip installed in the vehicle. The airflow over the duct naturally comes from the outside toward the fan. The slots are oriented to point outward such that when blowing is actuated the flow over the lip could be caused to separate on demand.



Figure 21: Leading Edge Flow Control Configuration in the Wind Tunnel

VI. Wind Tunnel and Static Experimental Results

A. Flow Visualization of Flow Control Concepts

In addition to collecting data from the force and moment balance, flow visualization was captured via video. This is helpful in communicating the overall phenomenon that is occurring. One of the most successful concepts was the Coanda trailing edge blowing at lower flight speeds and high blowing velocities. Two still frames from the video are shown in Figure 22 for a 35 ft/sec free-stream flow, with the vehicle tilted 20 degrees into the wind.

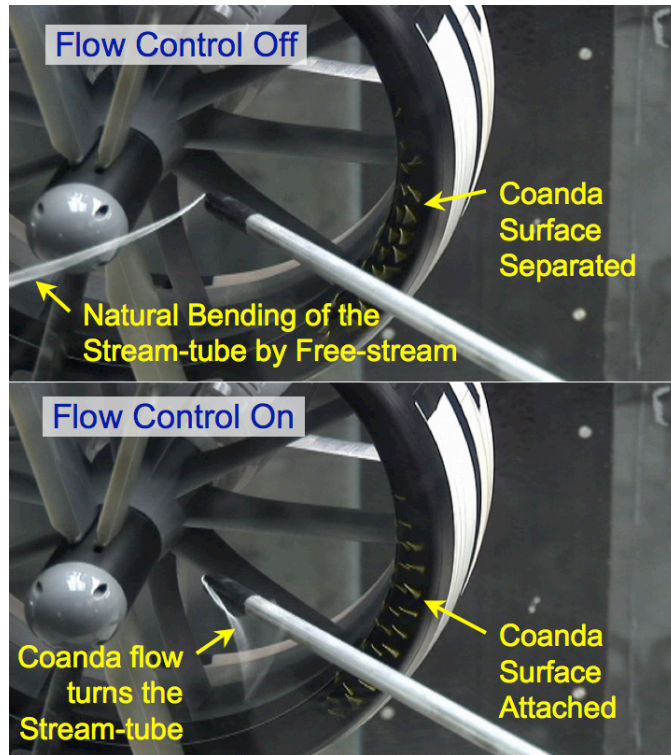


Figure 22: (top) No Blowing, Coanda Surface is Separated; (bottom) Steady Blowing at Highest Rate, Coanda Surface Fully Attached

In the first image, the Coanda blowing is turned off and the tufts on the Coanda surface at the duct exit are fluttering and imply separated flow. Also the tuft wand in the duct exit flow (“stream tube”) is being greatly influenced by the free-stream flow coming from the right, and is bending past the lower centerbody. In the second image, the highest steady blowing rate is in effect and the tufts on the Coanda surface are fully attached. This flow causes the whole stream tube to expand and turn upstream, as can be noted from the large angular change in the tuft wand.

Figure 23 shows similar visualization for the leading edge concept for a 35 ft/s free-stream flow at an angle of attack of -20 deg.

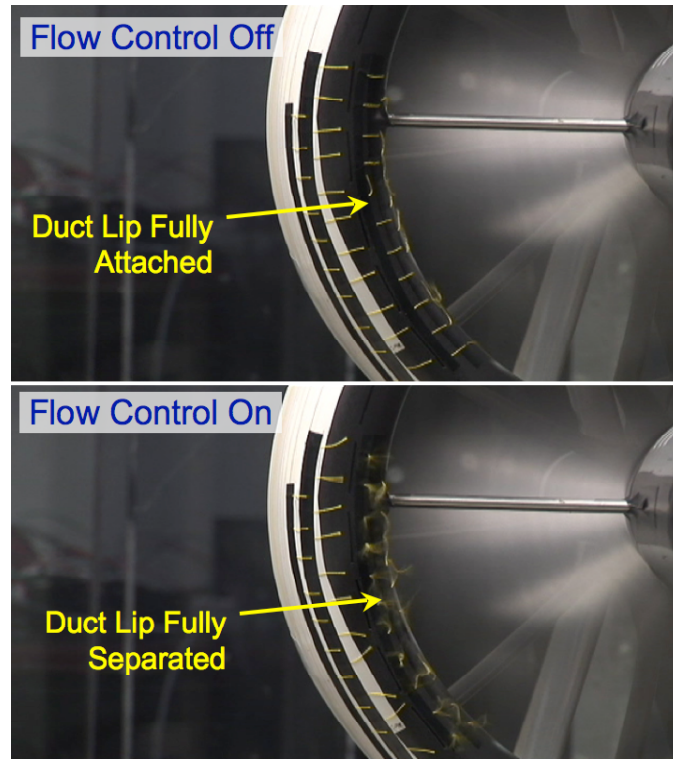


Figure 23: (top) No Blowing, Leading Edge is Attached; (bottom) Steady Blowing at Highest Rate, Duct Lip Fully Separated

The leading edge flow control has the opposite effect as compared to the trailing edge: when turned off the lip is fully attached, but when actuated, full flow separation is caused. When the flow is attached the thrust gained by the suction results in a nose-up pitching moment. When the flow is separated there is a loss of thrust and a decrease in pitching moment. While a loss of thrust sounds disadvantageous, a cross wind in hover can cause increased lift on the vehicle causing it to rise. If the vehicle is trying to maintain a fixed altitude, this ability to cancel the added lift from the cross wind through high bandwidth actuation could be desirable.

In summary, the flow visualization results showed that both flow control concepts achieved their desired intent, and can significantly affect the flow at high blowing levels. The remaining section will discuss the specific performance of each of these concepts, and how they affect the vehicle forces and moments.

B. Non-dimensional Approach for Ducted Fan Flow Control Data

Ducted fan vehicles present a unique problem for formulating non-dimensional coefficients for blowing momentum and vehicle forces and moments. Because the free-stream dynamic pressure used in most approaches goes to zero when the vehicle is hovering, a different approach is needed. An approach that can span hover to forward flight is optimal, and therefore must be based on some common parameter to both regimes. The fan tip speed or the flow induced through the duct are possible candidates. For vehicle forces and moments, the form typically used for propeller thrust coefficient will be applied to the normal and axial forces as well as the pitching moment. These are represented in Equations (5) through (7), respectively.

$$C_x = \frac{F_x}{\rho N^2 D^4} \quad (5)$$

$$C_z = \frac{F_z}{\rho N^2 D^4} \quad (6)$$

$$C_m = \frac{M_y}{\rho N^2 D^5} \quad (7)$$

where ρ is the air density, N is the rotational speed of the fan in revolutions per second, and D is the fan diameter. The blowing momentum coefficient typically used for fixed-wing flow control analysis [16] is :

$$c_\mu = \frac{\dot{m}_j U_j}{q_\infty S} \quad (8)$$

where \dot{m}_j is the jet mass flow, U_j is the jet speed, q_∞ is the free-stream dynamic pressure, and S is the wing planform area. Other researchers have used the fan tip speed to non-dimensionalize the blowing momentum coefficient for the ducted fan application [7]. While the fan tip speed offers a consistent way to normalize the data, it can be several times higher than the induced flow interacting with the flow control jets. To be more comparable to jet momentum coefficients for other applications, the speed of the flow inside the duct was chosen as a better reference for non-dimensional analysis. The flow induced through a ducted fan can be calculated from momentum theory as noted in [6] to be:

$$V_{induced} = \sqrt{\frac{T}{\rho A_{disc}}} \quad (9)$$

where T is the thrust, and A_{disc} is the area of the fan. The steady blowing momentum coefficient based upon the dynamic pressure of the induced flow then becomes:

$$c_\mu = \frac{\dot{m}_j U_j}{q_{duct} A_{duct}}, \quad q_{duct} = \frac{1}{2} \rho V_{induced}^2 \quad (10)$$

where A_{duct} is the projected area of the duct (diameter times chord) to be comparable with the planform area of a wing.

The synthetic jet oscillatory flow requires special treatment in deriving the equivalent blowing momentum coefficient. Farnsworth et. al. [17] have used a blowing momentum coefficient based on the total time-averaged momentum of the outstroke, \bar{I}_j , defined as:

$$\bar{I}_j = \frac{1}{\tau} \rho l_j w_j \int_0^\tau u_j^2(t) dt \quad (11)$$

where τ is the outstroke time (half the overall period), l_j is the slot length, w_j is the slot width, and u_j is the centerline velocity of the jet, as used in the definition for U_0 . Multiplying this value by the total number of jets to get the total momentum imparted and dividing by the induced dynamic pressure and area yields a comparable blowing momentum coefficient:

$$c_\mu = \frac{n \bar{I}_j}{q_{duct} A_{duct}} \quad (12)$$

The velocity ratio, as defined by Equation (13) and adapted from [18], is also of interest in flow control applications. It is defined relative to the induced velocity through the duct, as this is the velocity representative of the flow on which the control is acting for this application. For the tests performed the synthetic jets operated in the range of $V_R = 0.5$ to 1.0 , while the steady jets operated in the range of 1.5 to 5 .

$$V_R = \frac{U_0}{V_{induced}} \quad (13)$$

C. Numerical Results and Discussion

Static (hover) tests were performed for both the leading edge and trailing edge flow control configurations. While the concepts were designed to affect the vehicle horizontal flight at high angles of attack, the static capability of these flow control concepts was still of interest. The trailing edge Coanda flow control causes the duct flow to turn and thereby creates normal force. The normal force coefficient data versus jet momentum coefficient are shown in Figure 24. Data is presented in the form of deltas from the base vehicle aerodynamics since the jet blowing would be used as a control input to affect vehicle flight.

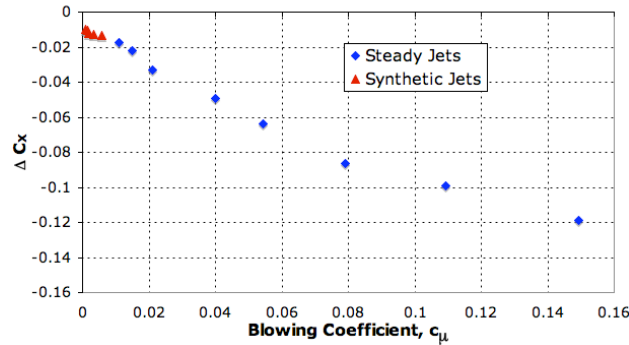


Figure 24: Static, Delta C_x vs Blowing Coefficient, Trailing Edge Flow Control

Because the steady blowing was powered by a separate supply of high-pressure air, higher blowing coefficient levels were explored to assess the full capability of the flow control concepts. Figure 24 shows that the synthetic jets were not able to attain the same level of blowing coefficient, but do follow the same trend in force generation, or even exceed the magnitude of the trend for steady blowing.

Figure 25 shows the effect on axial force of the trailing edge blowing. A positive delta to C_Z corresponds to lower thrust. As the flow is expanded by the Coanda blowing, it effectively increases the exit area of the duct and decreases the exit velocity, thereby lowering the net thrust.

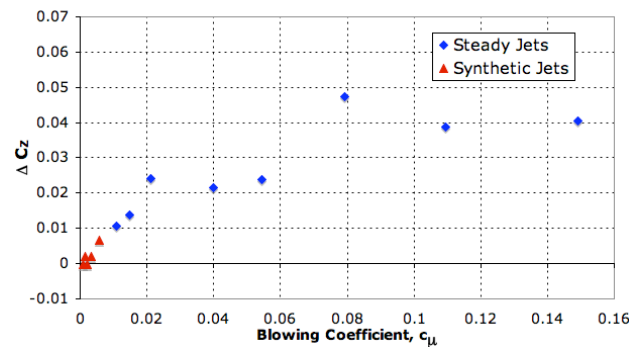


Figure 25: Static, Delta C_z vs Blowing Coefficient, Trailing Edge Flow Control

Figure 26 shows the effect of trailing edge blowing on pitching moment coefficient, the primary objective of the concept. Both steady blowing and synthetic jet blowing produce the intended behavior, with the steady blowing reaching larger values than the synthetic jets due to higher blowing coefficient levels. However, comparing the trends in the data, it would appear that the synthetic jets would affect pitching moment more for a given blowing coefficient.

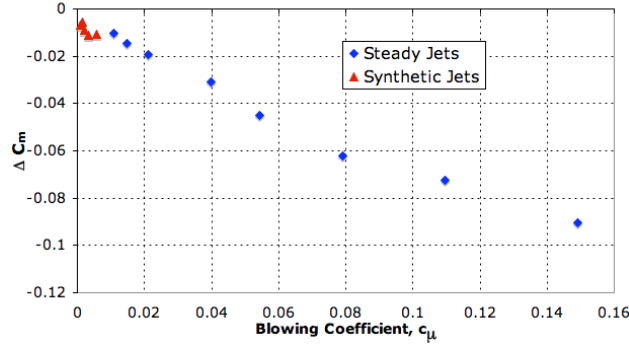


Figure 26: Static, Delta C_m vs Blowing Coefficient, Trailing Edge Flow Control

The leading edge flow control produced very little effect in static conditions. This is attributed to the duct lip design for smooth and efficient flow in hover. Effectively, the flow is too stable in hover for the synthetic or steady blowing to cause significant separation on the duct lip. This however does not imply that it will not succeed for its target application of high angle of attack forward flight.

Before discussing the deltas to force and moment coefficients due to flow control for flight conditions, it is important to gain a reference point of the underlying vehicle aerodynamics. The baseline vehicle coefficient data for a pitch sweep at 35 ft/s is shown in Figure 27.

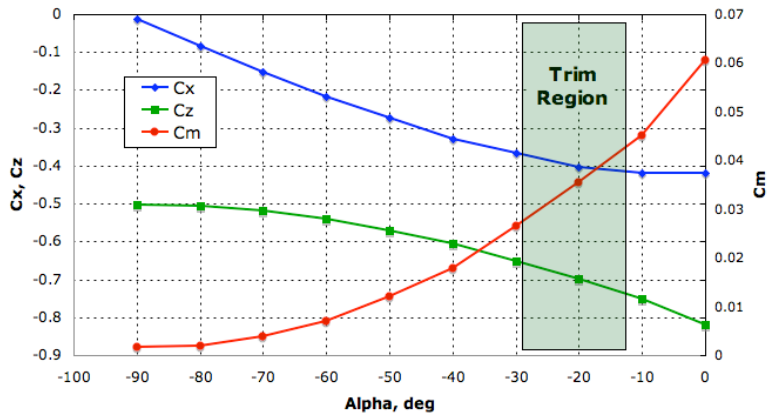


Figure 27: Baseline Vehicle Aerodynamic Data with Trim Region

Figure 27 shows the range of C_x , C_z , and C_m for the vehicle at a transition speed. The normal force and pitching moment are essentially zero at alpha of -90° (nose directly into the wind), and increase in magnitude as alpha increases. The axial force (thrust) is at its lowest magnitude at alpha of -90° (a pure axial climb orientation) and increases as well as the angle of attack increases. The ducted fan vehicle tilts into the wind to fly forward, and for this flight speed would pitch forward roughly -20° . At this condition it is necessary to trim the pitching moment to zero for equilibrium flight, so a goal of -0.04 change in pitching moment coefficient would be sufficient to accomplish this.

The wind tunnel test results for 17 ft/s and 35 ft/s (10 and 20 kt) are shown in Figure 28 through Figure 30.

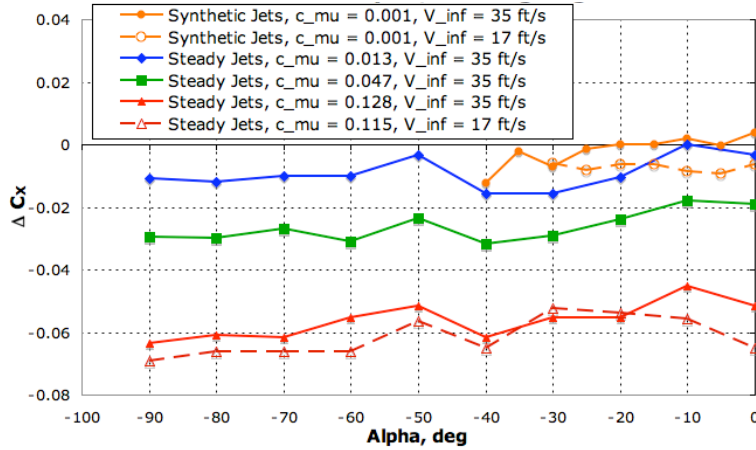


Figure 28: Forward Flight, Delta C_x vs Angle of Attack, Trailing Edge Flow Control

The normal force results show the expected progression in magnitude of the steady blowing results as blowing coefficient increases. The flow control also seems to be slightly more effective at slower flight conditions (17 ft/s), and this would be supported by the fact that the static effects for comparable blowing coefficient were even larger magnitude (~ 0.1). The same trend is observed in the synthetic jets, although the magnitude of the effects are much smaller due to the lower blowing coefficient.

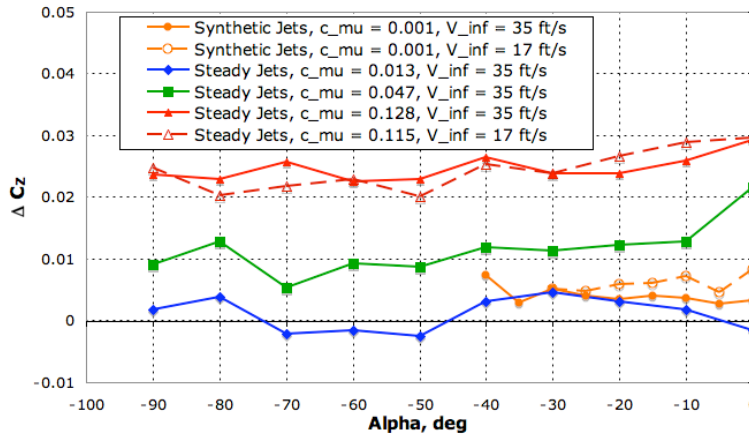


Figure 29: Forward Flight, Delta C_z vs Angle of Attack, Trailing Edge Flow Control

The axial force coefficient results show that the flow expansion results in some thrust loss for forward flight as it did in hover. One aspect to note is that the normal force produced by the flow control is more than double the amount of thrust force lost.

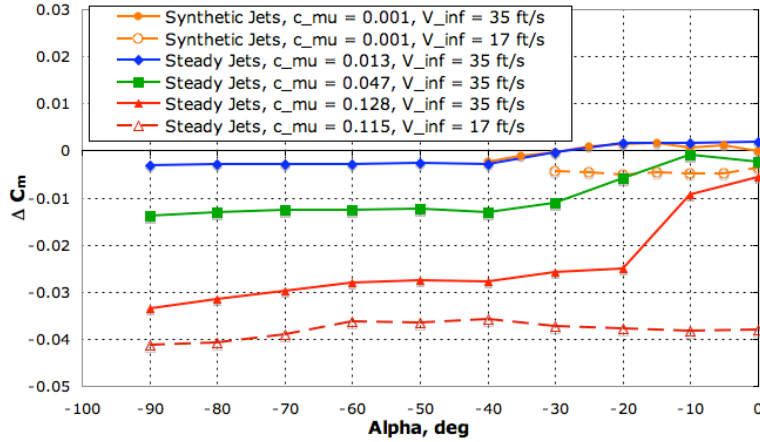


Figure 30: Forward Flight, Delta C_m vs Angle of Attack, Trailing Edge Flow Control

The trailing edge flow control does have a significant effect on vehicle pitching moment. For reference, the value of C_m is on the order of 0.04 for the trim angle of attack of -20° at 35 ft/s, and 0.035 for a trim angle of attack of -10° at 17 ft/s. The highest level of trailing edge blowing can completely cancel that moment for 17 ft/s flight and comes very close for 35 ft/s. It should be noted that this is a very high level of blowing and the synthetic jets are much less effective because of the substantially lower blowing coefficient levels. Again, the steady and synthetic jet flow control is more effective at a lower speed of forward flight, and the steady blowing results show a sudden decrease in effectiveness at high angles of attack (still close to trim region). This is due to the fact that the Coanda flow control is trying to turn the ducted fan flow in the opposite direction to the free-stream. As the free-stream flow becomes faster, it is more difficult to keep the Coanda flow attached. The conclusion is that the Coanda flow control is more effective at lower angles of attack where the turned flow is not directly competing with the free-stream.

While the leading edge flow control showed little effect for the hover condition, it was effective at producing separation on the duct lip for high angle of attack forward flight, as seen in the flow visualization section. The leading edge concept does not affect normal force, but does produce results in axial force and pitching moment as seen in Figure 31 and Figure 32.

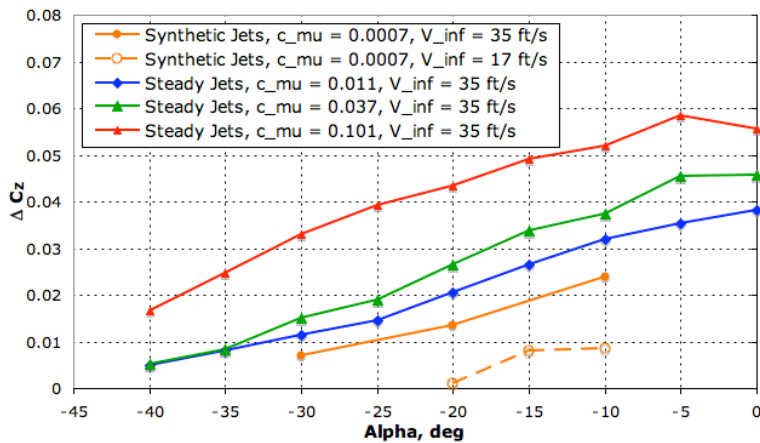


Figure 31: Forward Flight, Delta C_z vs Angle of Attack, Leading Edge Flow Control

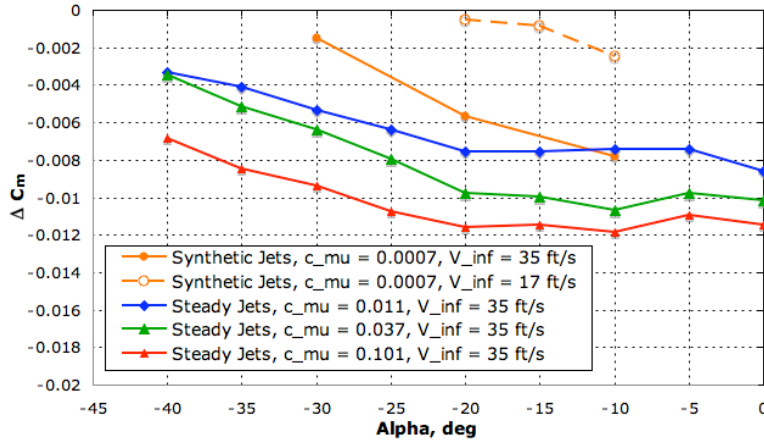


Figure 32: Forward Flight, Delta C_m vs Angle of Attack, Leading Edge Flow Control

While the trailing edge flow control concept corresponded to a control moment being created by generating a normal force, the leading edge concept shows the strong correlation between duct lip thrust and pitching moment. The separation caused on the lip results in thrust loss and decrease in pitching moment. The magnitudes of the deltas to pitching moment are roughly half of those seen in the steady trailing edge flow control, but the magnitudes increase with angle of attack whereas the trailing edge concept lost effectiveness at the conditions. These higher angles of attack are where the pitching moment is highest, and represent the area of greatest need for wind gust rejection. The deltas are smaller than the value needed for trim, so a solution based on this concept could only augment control and not be a complete solution for flight control actuation.

It should also be noted that the synthetic jets were much more effective in this configuration, but particularly at 35 ft/s instead of 17 ft/s. Even though the blowing coefficient for the synthetic jets is much lower than the steady blowing, the effects at 35 ft/s free-stream are comparable. What this suggests is that duct lip separation has more of a digital nature rather than a continuous behavior. In other words, there is a threshold that must be attained to cause separation through actuation, but further increases to actuation do not return as much benefit. This can be seen in the steady blowing as well, the greatest effect is seen going from no blowing to a blowing coefficient of 0.011. A blowing coefficient ten times greater only produces about 50% more effect on pitching moment. The lesson to be learned from this is that the nature of the flow one is trying to control is equally important or more important than the level of blowing being employed. In this particular application of causing separation in a flow that is somewhat unstable, synthetic jets were capable of creating a comparable effect but at a blowing coefficient that was a fraction of the steady blowing coefficient value.

VII. Conclusions

The flow control concepts were proven to be successful in producing aerodynamic forces and moments on a ducted fan, although some required high values of steady blowing to create significant responses. The flow control techniques presented could be used as control inputs for ducted fan flight control or augmenting wind gust rejection performance. Attaining high blowing momentum coefficients from synthetic jets is challenging since the time-averaged velocity is only a function of the outstroke: from bench test experiments it was seen that the time-averaged velocity was roughly one fourth of the peak velocity observed during the outstroke. The synthetic jets operated at lower blowing momentum coefficients than the steady jets tested, and in general the ducted fan application required more flow control authority than the synthetic jets could impart. However, triggering leading edge separation was one application where synthetic jets showed comparable performance to steady jets of much higher blowing coefficients. Identifying a flow condition that can be easily influenced by the momentum imparted from synthetic jets is critical.

Acknowledgments

The authors would like to thank the Air Force Research Laboratory (AFRL) for sponsorship of this research, specifically James D. Davis, the AFRL program manager of this Phase II SBIR contract. Thanks also go to colleagues at AVID LLC and the Center for Intelligent Material Systems and Structures (CIMSS) of Virginia Tech for their support with experiments and theoretical questions.

References

- [1] McMichael, J., A. Lovas, P. Plostins, J. Sahu, G. Brown, A. Glezer, "Microadaptive Flow Control Applied to a Spinning Projectile", AIAA Paper 2004-2512, 2nd AIAA Flow Control Conference, 28 June – 1 July 2004, Portland, Oregon, 2004
- [2] McCormick, B. W., *Aerodynamics of V/STOL Flight*, Dover Publications, 1999.
- [3] Fleming, Jonathan, Jones, Troy, Ng, Wing, Gelhausen, Paul, Enns, Dale. "Improving Control System Effectiveness for Ducted Fan VTOL UAVs Operating in Crosswinds." 2nd AIAA UAV Conference and Workshop & Exhibit, San Diego, CA, September 2003.
- [4] Graf, Will, Fleming, Jonathan, Ng, Wing, Gelhausen, Paul. "Ducted Fan Aerodynamics in Forward Flight." AHS International Specialists' Meeting on Unmanned Rotorcraft, Chandler, AZ, January 2005.
- [5] Graf, Will, "Effects of Duct Lip Shaping and Various Control Devices on the Hover and Forward Flight Performance of Ducted Fan UAVs", Masters Thesis, Virginia Tech, Blacksburg, VA, May 13, 2005.
- [6] Kondor, S., M. Heiges, "Active Flow Control For Control of Ducted Rotor Systems", AIAA Paper 2001-117, Proceedings, 39th AIAA Aerospace Sciences Meeting & Exhibit, January 8-11, 2001, Reno, Nevada, 2001.
- [7] Kondor, S., W. Lee, R. Englar, M. Moore, "Experimental Investigation of Circulation Control on a Shrouded Fan", Paper AIAA-2003-3409. Proceedings, 33rd Fluid Dynamics Conference, June 23-26, 2003, Orlando, FL.
- [8] Kondor, S., "Further Experimental Investigation of Circulation Control Morphing Shrouded Fan", Paper AIAA 2005-639, Proceedings, 43rd AIAA Aerospace Sciences Meeting and Exhibit, Reno, NV, 10 - 13 January 2005.
- [9] Fung, P. H., M. Amitay, "Control of a Miniducted-Fan Unmanned Aerial Vehicle Using Active Flow Control", *Journal of Aircraft*, Vol. 39, No. 4, 2002, pp 561-571.
- [10] Smith, B. L., G. W. Swift, "A Comparison Between Synthetic Jets and Continuous Jets", *Experiments in Fluids*, Vol. 34, 2003, pp 467-472.
- [11] Gomes, L. D., W. J. Crowther, and N.J. Wood, "Towards a practical piezoceramic diaphragm based synthetic jet actuator for high subsonic applications – effect of chamber and orifice depth on actuator peak velocity", AIAA Paper 2006-2859, Proceedings of 3rd AIAA Flow Control Conference, San Francisco, California, 5-8 June 2006.
- [12] Sharma, R. N., "Fluid-Dynamics-Based Analytical Model for Synthetic Jet Actuation", *AIAA Journal*, Vol. 45, No. 8, August 2007, pp. 1841-1847.
- [13] Holman, R., Y. Utkurkar, R. Mittal, B. L. Smith, and L. Cattafesta, "Formation Criterion for Synthetic Jets", *AIAA Journal*, Vol. 43, No. 10, October 2005, pp. 2110-2116.
- [14] Anderson, W. K. and Bonhaus, D. L., "An Implicit Upwind Algorithm for Computing Turbulent Flows on Unstructured Grids," *Computers and Fluids*, Vol. 23, No. 1, 1994, pp. 1–22.
- [15] O'Brien, D., *Analysis of Computational Modeling Techniques for Complete Rotorcraft Configurations*, Ph.D. thesis, Georgia Institute of Technology, 2006.
- [16] Englar, R. J., "Overview of Circulation Control Pneumatic Aerodynamics: Blown Force and Moment Augmentation and Modification as Applied Primarily to Fixed-Wing Aircraft", Chapter 2, *Applications of Circulation Control Technology*, American Institute of Aeronautics and Astronautics, Reston, VA, 2006.
- [17] Farnsworth, J. A. N., J. C. Vaccaro, and M. Amitay, "Active Flow Control at Low Angles of Attack: Stingray Unmanned Aerial Vehicle", *AIAA Journal*, Vol. 46, No. 10, October 2008, pp. 2530-2544.
- [18] Zhong, S. M. Jabbal, H. Tang, L. Garcillan, F. Guo, N. Wood, C. Warsop, "Towards the Design of Synthetic-jet Actuators for Full-scale Flight Conditions, Part 1: The Fluid Mechanics of Synthetic-jet Actuators", *Flow, Turbulence and Combustion*, Vol. 78. No. 3-4, 2007, pp. 283-307.